



# A machine learning approach to automate ductile damage parameter selection using finite element simulations

A.N. O'Connor<sup>a,b,\*</sup>, P.G. Mongan<sup>a,c</sup>, N.P. O'Dowd<sup>a,b,c</sup>

<sup>a</sup> School of Engineering, University of Limerick, Ireland

<sup>b</sup> Bernal Institute, University of Limerick, Ireland

<sup>c</sup> Confirm Smart Manufacturing Research Centre, Ireland

## ARTICLE INFO

Dataset link: <https://doi.org/10.5281/zenodo.7686217>

### Keywords:

Machine learning

Bayesian optimisation

Ductile damage

Parameter selection

## ABSTRACT

Ductile damage models require constitutive model parameter values that are difficult to derive experimentally or analytically. The calibration procedure for ductile damage model parameters, typically performed manually, is labour-intensive. In this work we detail a fully autonomous framework that integrates Bayesian optimisation and finite element analysis to identify ductile damage model parameters. The framework detailed here selects ductile damage model parameters from inputs that can be derived from a simple tensile test. This framework has been successfully deployed to three datasets of P91 material tested at ambient (20 °C) and higher (500 °C) temperatures. The Bayesian optimisation derived material model parameters result in simulated output with less than 2% error compared to experimental data. This research demonstrates that algorithm hyperparameters can significantly affect the Bayesian optimised ductile damage parameter values resulting in non-unique ductile damage parameters. We show that the non-unique solutions can be further assessed using a second test geometry.

## 1. Introduction

The tensile test is a standard test method (Anon, 2019) that provides information about the mechanical properties of metallic materials. In cases where experimental data are limited finite element (FE) simulations can be used to simulate the mechanical behaviour of materials and examine hypotheses that cannot be experimentally investigated. The FE method offers a level of detail not obtainable from analytical solutions but is relatively computationally expensive and ultimately relies on experimental data for validation. Gurson (1977) developed a constitutive model to describe void nucleation and growth in ductile metals, that was later improved by Tvergaard and Needleman (1984) and is now commonly referred to as the Gurson–Tvergaard–Needleman (GTN) model.

The yield surface of the GTN model response is described in Eq. (1), where  $q$  is the Mises stress,  $\sigma_y$  is the material yield stress,  $f$  is the current void volume fraction (the ratio of the volume of voids to the total material volume),  $p$  the hydrostatic pressure and  $q_1$ ,  $q_2$ , and  $q_3$  are material parameters,

$$\Phi = \left( \frac{q}{\sigma_y} \right)^2 + 2q_1 f \cosh \left( -\frac{3}{2} \frac{q_2 p}{\sigma_y} \right) - (1 + q_3 f^2) = 0 \quad (1)$$

The rate of change of the void volume fraction,  $f$ , is described by Eq. (2) where  $\dot{f}_n$  and  $\dot{f}_g$  represent the void nucleation rate and void growth rate, respectively,

$$\dot{f} = \dot{f}_n + \dot{f}_g. \quad (2)$$

The void growth rate,  $\dot{f}_g$ , is obtained from conservation of mass,

$$\dot{f}_g = (1 - f) \dot{\epsilon} : I, \quad (3)$$

where  $\dot{\epsilon}$  is plastic strain rate. The void nucleation rate,  $\dot{f}_n$ , is given by Eq. (4), where  $\epsilon_m^p$  is the plastic strain of the unvoided (matrix) material, and  $f_N$ ,  $S_N$  and  $\epsilon_N$ , are material parameters.

$$\dot{f}_n = \frac{f_N}{S_N \sqrt{2\pi}} \exp \left[ -\frac{1}{2} \left( \frac{\epsilon_m^p - \epsilon_N}{S_N} \right)^2 \right] \epsilon_m^p \quad (4)$$

The evolution of  $\epsilon_m^p$  is assumed to be governed by the equivalent plastic work expression (Systemes, 2021). Since, the void volume,  $f$ , is defined through a rate equation, the initial void volume fraction,  $f_0$ , must also be defined. Constitutive models such as the GTN model are generally used in conjunction with FE simulation to better represent the mechanical behaviour of metals under high strain conditions when

\* Corresponding author at: School of Engineering, University of Limerick, Ireland.

E-mail address: [alison.oconnor@ul.ie](mailto:alison.oconnor@ul.ie) (A.N. O'Connor).

damage mechanisms are important (Abbassi et al., 2013; Chahboub and Szavai, 2019; Zhang et al., 2021).

The GTN model is complex and requires constitutive model parameter values that are difficult to derive experimentally or analytically. In the case of the GTN model the constitutive model contains a mix of empirical parameters ( $q_1, q_2, q_3$ ) and non-empirical ( $f_0, f_N, s_N, \epsilon_N$ ) parameters. The non-empirical parameters, have been derived from physically-based microscale finite element simulations and are associated with the physical properties of the material (Brocks et al., 1995). Attempts to evaluate some non-empirical parameter values experimentally (Weislik, 2016; Maire et al., 2008) are considered “largely subjective” in terms of result outputs (Zhang et al., 2021). The relationship between GTN model parameters is further complicated by parameter interaction effects where the ‘best’ fit to experimental data can be found from multiple parameter combinations (Kiran and Khandelwal, 2014; Zhang et al., 2021). The parameters are typically estimated by conducting numerical simulations, manually iterating the relevant parameter value, and matching the simulation result to experimental data (Brocks, 2018).

Machine learning (ML) is a term used to describe algorithms and/or statistical models that allow computers to select the best method of progression in a problem, without human interaction or explicit programming (Bikmukhametov and Jäschke, 2020). ‘Machine Learning is the study of computer algorithms that improve automatically through experience’ (Ertel, 2017); essentially the algorithm teaches itself to recognise patterns of behaviour between data inputs and outputs, which can be generalised to predict output when inputs are unknown. Calibrating a ductile damage model, such as the GTN model, is difficult because while the inputs (constitutive model parameters) and target outputs (data in a tensile test) are known, the functional relationship between the model parameters and the material mechanical response generated by FE must be calculated numerically. ML algorithms, informed directly by experimental and/or simulation data, have been successfully employed to solve numerous engineering problems across a wide range of engineering applications. Mongan et al. (2022) successfully identified the ultrasonic welding parameters (inputs) that maximise the lap shear strength (output) of a dissimilar composite component based on experimental data. Meanwhile Liu et al. (2020) predominately used FE generated data, supported by a limited number of experiments, to assess how specimen geometry and loading correlated to the fracture toughness of a ceramic material. Hegde and Rokseth (2020) showed that a variety of ML methods could support engineering risk identification and noted that they were actively used within the automotive and construction industries. ML has recently gained traction in the field of constitutive material modelling by offering advantages in generality and efficiency compared to FE simulations alone. Schulte et al. (2023) used ML to estimate large parameter values for a large deformation and damage phenomenological model applied to FE models. In Schulte et al. (2023) the authors state that it is difficult to calibrate models with large numbers of parameters, particularly when the physical interpretation of the parameter(s) is not clear. Additional literature combining ML and constitutive models include works by Li et al. (2023), which investigated a coupled strain-rate and temperature dependent constitutive model, and Abbassi et al. (2023), which implements a fully coupled hydraulic-mechanical continuum damage model for fluid injection on fractured reservoirs.

Artificial neural networks (ANNs), Bayesian optimisation (BO) and genetic algorithms (GA) are among the most popular ML algorithms for engineering applications (Nasiri et al., 2017). Indeed, many of the works discussed here used an ANN model (Schulte et al., 2023; Li et al., 2023; Abbassi et al., 2023; Mongan et al., 2022). A significant dataset is required to ‘train’ an ANN model to recognise correlations and relationships between input and output parameters and this can be computationally expensive. Of the ML algorithms used in literature, BO has been shown to outperform other ML algorithms in solving similar parameter inference problems (Borowska et al., 2022;

Gunn et al., 2022). BO is an active learning method that optimises an objective function using probabilistic theory (Liang et al., 2021). A more technical description of BO is provided in Section 3 but for the purposes of this introduction it is sufficient to note that it is the versatility of BO that makes it an attractive method for solving a wide variety of engineering challenges. BO has been successfully applied to research such as: material design (Zhang et al., 2020; Chuaqui et al., 2021), cardiac mechanics (Borowska et al., 2022), light emission for thin films (Wankerl et al., 2022) and manufacturing process improvements (Mongan et al., 2022; Gunn et al., 2022). A common application of BO is ANN hyperparameter selection (Dewancker et al., 2016; Mongan et al., 2022; Bikmukhametov and Jäschke, 2020; Ghavamian, 2021) as it enables programmers to more quickly identify hyperparameter values that maximise both the speed and accuracy of the ANN model. ANNs are also a popular algorithm choice and have been applied to various engineering challenges including constitutive model parameter evaluation (Abendroth and Kuna, 2006; Abbassi et al., 2013; Chahboub and Szavai, 2019; Chen et al., 2021). However, as stated earlier, a key drawback of ANNs is the significant number of data required to ‘train’ the model which can be computationally expensive.

Ryan et al. (2022) recently used BO to identify material parameters in a viscoplastic material model and found that the optimised parameters provided ‘superior’ agreement to experimental measurements compared to FE simulations. To derived generalised model parameters Ryan et al. (2022) preformed FE simulations of six types of experimental blast test, repeating these simulations for several constitutive equations. Using a leave-one-out validation method Ryan et al. (2022) showed that the optimised parameter values, despite being non-unique, resulted in reasonable agreement between experimental data and FE simulation for a seventh type of blast experiment (i.e. an experiment that was not considered in the ML algorithm). This work demonstrates how BO can be used to automatically identify model parameters by comparing experimental data to simulated results. The purpose of this work is to reduce the time associated with deriving GTN parameter values and ensure minimal user intervention through the use of BO combined with finite element analysis. A similar approach to that used in Ryan et al. (2022) has been adopted, but in this case the approach is applied to ductile damage rather than the rate sensitive viscoplasticity constitutive models examined in Ryan et al. (2022).

## 2. Experimental data

Three experimental tensile test results are shown in Fig. 1 for the material of interest (P91, a piping steel). Dataset 1 represents the average of two tensile tests both conducted at room temperature ( $\approx 25^\circ\text{C}$ ) with a crosshead displacement 0.375 mm/min. Dataset 2 represents a single test conducted at room temperature with a crosshead displacement of 1.5 mm/min. Dataset 3 represents a single test conducted at  $500^\circ\text{C}$  at a fixed crosshead displacement of 1.5 mm/min.

### 2.1. Assessment of linear data

Two material parameters are required in the linear (elastic) region: Young’s modulus,  $E$ , and yield strength,  $\sigma_y$ . As the choice of  $\sigma_y$ , influences the value of  $E$ , these are obtained by an iterative process (outside the BO framework). The region over which  $\sigma_y$  is evaluated is solved iteratively and Young’s modulus,  $E$ , is calculated by employing linear regression to fit all data below the selected yield strength. Fig. 2 shows the elastic-region result for each of the three datasets.

The true stress–true strain relationship is valid only to the point of ultimate tensile strength,  $\sigma_{UTS}$ , as specimen necking occurs after the UTS is reached and the deformation is no longer uniform. In this work for  $\sigma > \sigma_{UTS}$ , the true stress is interpolated from the values for  $\sigma \leq \sigma_{UTS}$ , with the understanding that, in the absence of damage, the true stress always increases with increasing strain. Here, a linear relationship between true stress and true strain, with slope  $m$ , for  $\sigma \geq$

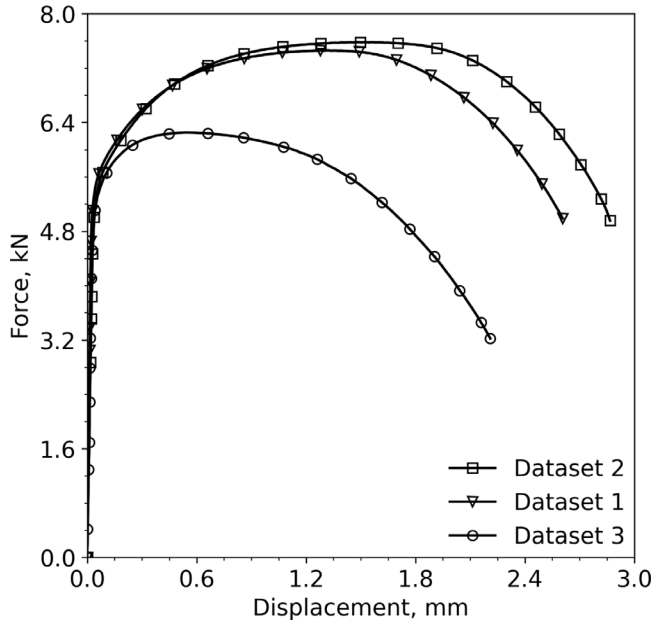


Fig. 1. Experimental tensile test results for P91 material at test temperatures of 20 °C (Datasets 1 and 2) and 500 °C (Dataset 3). Note: Markers are used for data visibility purposes only. High data acquisition rate was used during testing.

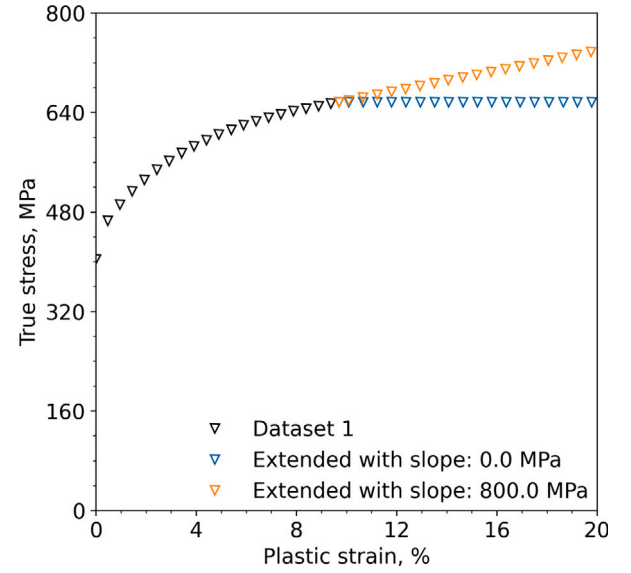


Fig. 3. True stress-plastic strain relationship for dataset 1. Test data are shown using black markers. Two parameter values (minimum and maximum) are distinguished using coloured markers.

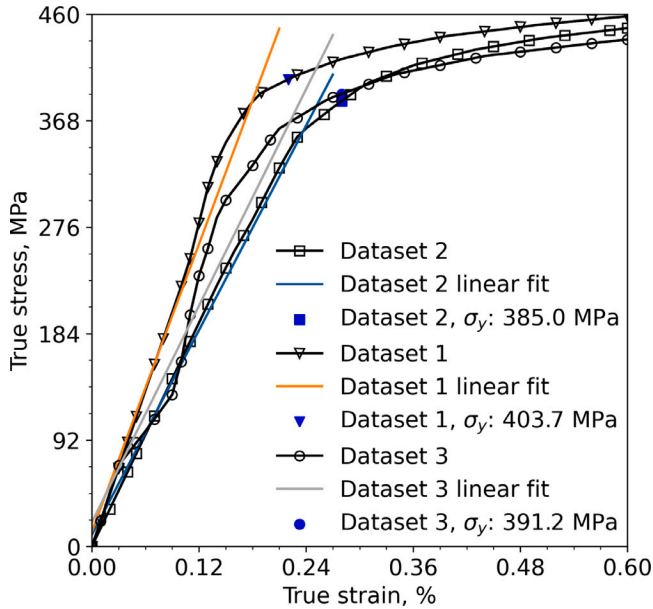


Fig. 2. True stress-true strain elastic region results for three experimental tests.

$\sigma_{UTS}$  is assumed. The slope of the extrapolated line, parameter  $m$ , is one of the eight parameters determined by the BO framework. The range of  $m$  is dependent on the material; the minimum value is assumed to be zero (as in Fig. 3), representing perfectly plastic behaviour. The maximum value of  $m$  is selected by an iterative process. A linear fit is applied to a number of data points (data groups), up to a maximum of

five data points preceding  $\sigma_{UTS}$ . The resulting maximum value of  $m$  of any data group is selected to represent the maximum allowable value of  $m$ . Listing 1 (see Appendix Supplementary information), is an exemplar demonstrating the process used to identify the maximum boundary. The true stress-true strain curve is then extrapolated linearly beyond  $\sigma_{UTS}$  with a slope  $m$ , as shown in Fig. 3 for Dataset 1.

There are a total of seven parameters in the GTN ductile damage model to fit using BO:  $q_1$ ,  $q_2$ ,  $q_3$ ,  $S_N$ ,  $f_N$ ,  $\epsilon_N$ , and  $f_0$  (see Section 1). Including the slope of the true stress-true strain curve for  $\sigma > \sigma_{UTS}$ ,  $m$ , gives a total of eight parameters.

### 3. The Bayesian optimisation framework

The goal of BO is to find the global minimum of an unknown function. There are two key ingredients to a BO framework: a surrogate model and a loss function. The surrogate model, sometimes called a probabilistic model, describes the BO's current knowledge about the unknown function based on observed data. The loss function describes how well the previously observed data are optimised (i.e. converging towards a global minimum) (Shahriari et al., 2016). The surrogate model and loss function work jointly with an acquisition function, which controls how the BO explores the parameter space. The surrogate model,  $f(x)$ , is determined using Gaussian process regression (GPR) on inputs,  $x$ , the observed data related to the unknown function. A Gaussian process is a collection of random variables, many of which have consistent, joint Gaussian distributions, specified by the covariance function (Rasmussen, 2004; Rasmussen and Williams, 2006) (see Section 3.1 for further details on the covariance function).

The probability distribution generated by GPR is based on a ranking system, where input  $x$  is evaluated as  $f(x)$  and  $f(x)$  is ranked in terms of its performance relative to the loss function. In this work the loss function is the mean average percentage error (MAPE) which quantifies the similarity between simulated and experimental data (see Section 3.2 for further detail). To minimise the loss function the L-BFGS-B optimisation

**Table 1**

Parameter space representing the minimum and maximum boundary for each parameter.

Dataset	Parameter	Minimum	Maximum
1–3	$q_1$	$9.00 \times 10^{-1}$	1.60
1–3	$q_2$	$9.00 \times 10^{-1}$	1.10
1–3	$q_3$	$8.10 \times 10^{-1}$	2.56
1–3	$\epsilon_N$	$2.50 \times 10^{-1}$	$4.00 \times 10^{-1}$
1–3	$f_N$	$3.00 \times 10^{-1}$	$9.00 \times 10^{-2}$
1–3	$s_N$	$1.00 \times 10^{-1}$	$2.00 \times 10^{-1}$
1–3	$f_0$	$1.30 \times 10^{-3}$	$1.50 \times 10^{-3}$
1	$m$	0	800
2	$m$	0	1100
3	$m$	0	800

algorithm (Zhu et al., 1997) is used. This algorithm uses historical gradient evaluations of  $f(x)$  to construct an approximation of the unknown function.

In order to set reasonable bounds to the possible solutions of the problem, a parameter space is defined, within which the BO algorithm searches for values. The parameter space of the current problem is defined in Table 1 for the GTN parameters, based on information in the literature for similar materials (Kiran and Khandelwal, 2014; Meade, 2020; Systemes, 2021). The process used to define the bounds for  $m$  is outlined in detail in Section 2.

### 3.1. The covariance function

The covariance function used in the GPR has significant influence on the shape and characteristics of the surrogate function (Mongan et al., 2022). In this work a covariance function,  $k(x_i, x_j)$ , which uses a combination of the Matérn, Constant and White noise (White) functions, as shown in Eq. (5),

$$k(x_i, x_j) = \text{Matérn} + \text{Constant} \times \text{White}, \quad (5)$$

is implemented. As the shape and/or characteristics of the function are unknown this covariance kernel is designed to account for shifts in mean position (Constant), noise (White) and to model potentially multiple minima positions (Matérn). The Matérn covariance function is defined in Eq. (6) (Pedregosa et al., 2011),

$$k(x_i, x_j) = \frac{1}{\Gamma(\nu)2^{\nu-1}} \left( \frac{\sqrt{2\nu}}{l} d(x_i, x_j) \right)^\nu K_\nu \left( \frac{\sqrt{2\nu}}{l} d(x_i, x_j) \right), \quad (6)$$

where  $x_i$  and  $x_j$  are input points,  $d$  is the Euclidean distance,  $K_\nu$  is a modified Bessel function and  $\Gamma$  is the gamma function. The Constant covariance function, is defined in Eq. (7) (Pedregosa et al., 2011),

$$k(x_i, x_j) = C; \forall x_i, x_j, \quad (7)$$

where  $C$  is a constant. The White covariance function is defined in Eq. (8),

$$k(x_i, x_j) = \sigma^2 \delta_{ij}, \quad (8)$$

where  $\sigma^2$  is constant and  $\delta_{ij}$  the Kronecker delta function. In this work the following kernel hyperparameters are fixed:  $\nu = 1$ ,  $l = 1$ ,  $C = 1$ ,  $\sigma^2 = 1$ .

### 3.2. The loss function (MAPE)

The aim of this work is to minimise the difference between experimental test data and simulation outputs generated from a finite element (FE) analysis of the problem. The experimental data are measures of applied load and specimen extension. In this work mean average percentage error (MAPE), Eq. (9), is used to measure the similarity between experimental data and simulated output,

$$\text{MAPE} = \frac{100}{n} \sum_i^n \left| \frac{P_{exp}^i - P_{sim}^i}{P_{exp}^i} \right|. \quad (9)$$

**Table 2**

Design of experiments array for 8 parameters with each parameter at 2 levels.

	$P_1$	$P_2$	$P_3$	$P_4$	$P_5$	$P_6$	$P_7$	$P_8$
1	1	1	1	1	1	1	1	1
2	1	1	1	1	1	2	2	2
3	1	1	2	2	2	1	1	1
4	1	2	1	2	2	1	2	2
5	1	2	2	1	2	2	1	2
6	1	2	2	2	1	2	2	1
7	2	1	2	2	1	1	2	2
8	2	1	2	1	2	2	2	1
9	2	1	1	2	2	2	1	2
10	2	2	2	1	1	1	1	2
11	2	2	1	2	1	2	1	1
12	2	2	1	1	2	1	2	1

Here  $P_{exp}^i$  represents each experimental load data point,  $P_{sim}^i$  is the corresponding simulation load and  $n$  the number of data points. MAPE provides an average measure of error over the full dataset with all data points equally weighted.

### 3.3. The acquisition function, $\alpha$

In this work the upper confidence bound (UCB) acquisition function is employed. The UCB, Eq. (10), identifies the new parameters through a weighted sum of the surrogate function, where  $\mu(x)$  is the mean, and  $\sigma(x)$ , the variance, respectively (Shahriari et al., 2016; De Ath et al., 2021),

$$\alpha_{UCB}(x) = \mu(x) + B \sigma(x). \quad (10)$$

Exploration and exploitation balance how the BO model searches the parameter space. When  $B$  is large (e.g.  $B > 2$ ) the acquisition function operates in exploratory mode; reducing the weight switches the model to exploitation mode. In exploration mode the new assessment point is chosen from areas of large uncertainty, typically this represents parameter values that differ significantly from the previous iteration; exploitation mode generally returns a new assessment point close to that tested previously (where the surrogate and objective functions are well aligned). In our work we have taken  $B = 2.5$ , which enforces an exploratory based assessment. An exploratory based assessment is more likely to achieve the target global minimum at the cost of longer convergence/computation time (De Ath et al., 2021).

In addition to the weight,  $B$ , the acquisition function has two further hyperparameters: the number of random samples,  $N_R$ , and the number of optimisation samples,  $N_O$ .  $N_R$  controls the size of the array over which the range of possible inputs are distributed – increasing  $N_R$  increases the precision of the GPR, thus reducing uncertainty.  $N_O$  defines how many evaluations of the acquisition function are conducted and controls the level of uncertainty in the acquisition function – increasing  $N_O$  makes the optimisation process more robust.

### 3.4. Initialising the BO framework

BO requires a database of initial evaluated data within the parameter space. We use a design of experiment (DoE) approach, (Uy and Telford, 2009; Fraley et al., 2020), to provide the initial evaluated data. DoE maximises the statistical significance of results with a minimised number of experiments. Table 2 shows a DoE array for 12 initial finite element simulations based on the maximum and minimum parameter space values, where values of 1 and 2 in Table 2 represent the minimum and maximum parameter bounds, respectively.

Fig. 4 shows a flowchart describing the DoE procedure. As illustrated in Fig. 4, the user first defines the parameter space (here shown in Table 1). A DoE array (Table 2) is defined and the DoE array is modified so that the minimum and maximum values (i.e. 1 and 2)

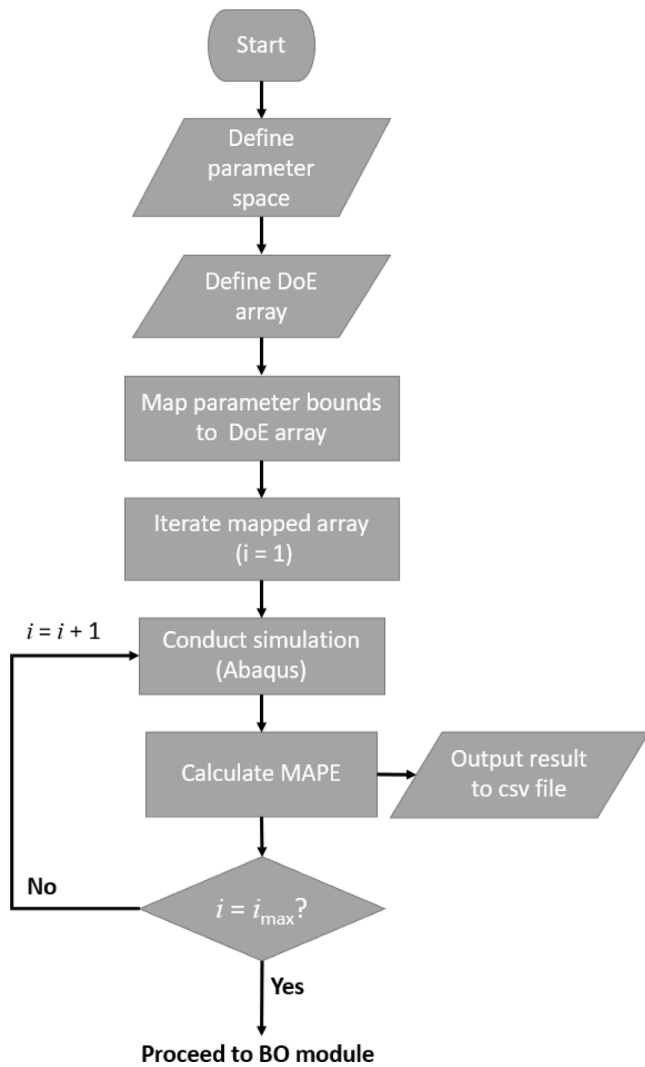


Fig. 4. Flowchart demonstrating the design of experiments code procedure (prior to Bayesian optimisation).

are replaced by the user-defined parameter values (see Table 1). A finite element simulation is conducted for each row of the DoE array ( $i_{max}$ ) is the number of (virtual) experiments in the DoE array, here 12. Results from the simulation are processed (see Section 4 for details) and MAPE is calculated (Section 3.2) by comparing the simulated output to experimental data. After each analysis,  $i$ , the parameter values and the associated error measurement are appended to a csv file.

### 3.5. Implementation of the BO model

The output of the DoE in Fig. 4 (a csv file of parameter values and error measurements) is used to initialise the Bayesian optimiser. Fig. 5 outlines the method: The DoE data are analysed by the GPR to create an initial surrogate model. GPR outputs are then provided to the acquisition function which identifies new parameter values based on ranking the DoE data. A new finite element simulation, using parameter values obtained from the acquisition function, is then conducted. Again simulation data is compared to the experiment and the MAPE is calculated. Acquisition function parameter values and error measurement data are appended to the existing csv file. The algorithm iterates until the MAPE is less than 2% or a maximum number of iterations ( $j_{max}$ ) is achieved. In the current approach, to ensure that BO is always carried out the analysis is not terminated if  $MAPE < 2\%$  in the DoE.

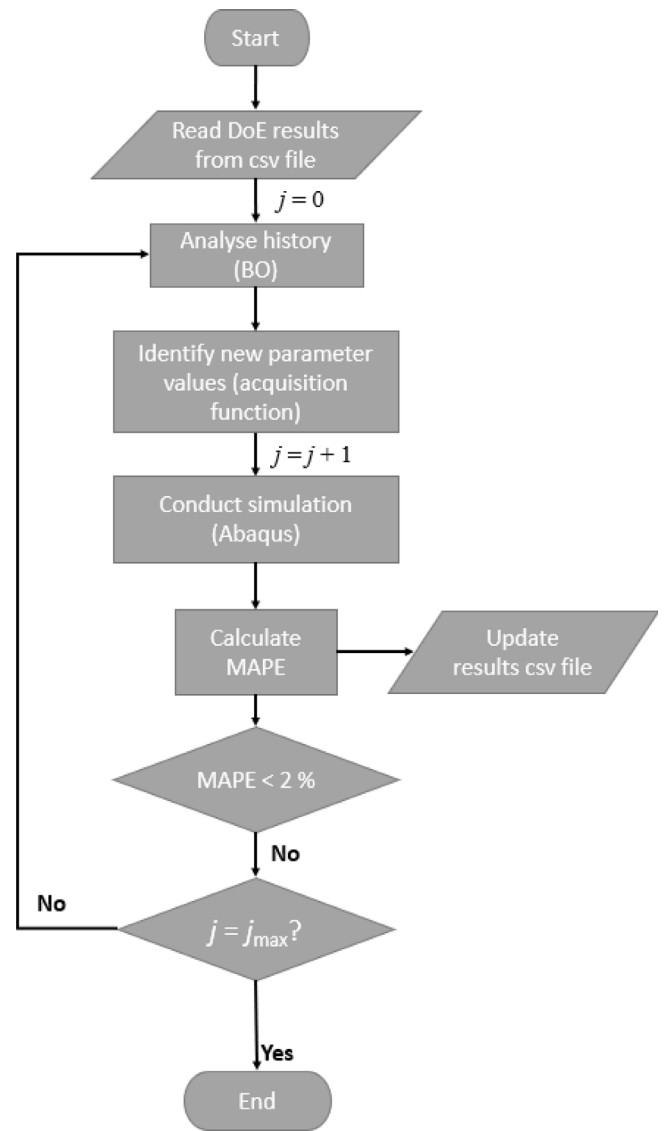


Fig. 5. Flowchart depicting code procedure for Bayesian optimisation.

## 4. FE modelling of tensile tests

Finite element modelling was conducted using Abaqus/Explicit (Systemes, 2021) (Explicit). Explicit uses a dynamic solver, and here a mass scaling factor of 10 is used to reduce computation time (Systemes, 2021). The model was meshed using 4664 linear, reduced integration axisymmetric (CAX4R) elements. The smallest element size is 0.09 mm.

The experimental tensile test geometry is shown in Fig. 6. The use of a 2D axisymmetric model reduces the computational expense of the simulation. Following the approach in Systemes (2021) for modelling of necking, a small imperfection is introduced at the bottom right hand corner of the model, as shown in Fig. 6, to provide a site for specimen necking at large displacements. The imperfection is modelled as an isosceles right-angled triangle with a fixed length of 0.025 mm.

Non-linear material behaviour is provided as a set of plastic strain versus true-stress values (as in Fig. 3). To model material degradation due to ductile damage the GTN model was applied, as discussed in Section 1.



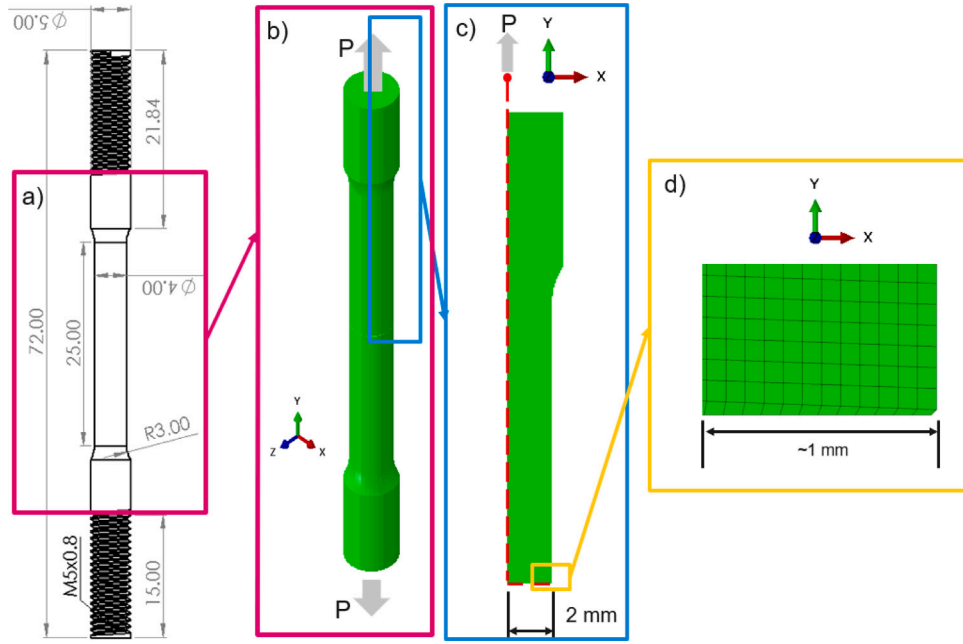


**Fig. 6.** (a) Tensile specimen (all dimensions in mm) (b) 3D visualisation of the test specimen (c) axisymmetric finite element model; (d) is an inset to (c) where a small imperfection is modelled to ensure failure occurred in the midsection of the gauge length.

**Table 3**  
Bayesian optimisation framework parameter values for each of the three datasets analysed.

Parameter	Dataset 1	Dataset 2	Dataset 3
$N_O$		500	
$N_R$		50,000	
$q_1$	1.332	1.168	1.182
$q_2$	$9.952 \times 10^{-1}$	$9.667 \times 10^{-1}$	$9.699 \times 10^{-1}$
$q_3$	2.295	1.407	2.001
$\epsilon_N$	$2.900 \times 10^{-1}$	$3.467 \times 10^{-1}$	$3.720 \times 10^{-1}$
$S_N$	$1.671 \times 10^{-1}$	$1.856 \times 10^{-1}$	$1.214 \times 10^{-1}$
$f_N$	$3.869 \times 10^{-2}$	$8.481 \times 10^{-2}$	$4.706 \times 10^{-2}$
$f_0$	$1.370 \times 10^{-3}$	$1.340 \times 10^{-3}$	$1.310 \times 10^{-3}$
$m$	534.1	725.4	421.4
MAPE	1.563	1.827	1.799
$N_j$	140	110	100

## 5. Results and discussion

The procedure described in Fig. 5 is applied to the three datasets. The assessment of each dataset is independent of one another. Typically, one complete analysis requires 150 finite element simulations and takes approximately 4 h on a standard laptop with four Intel i7 CPUs and 32 GB of RAM.

The comparison between data and simulation is shown in Fig. 7 for the three datasets. Fig. 7(a) (Dataset 1) shows that the simulated output is in good agreement with experimental data over the full displacement range although simulated forces are slightly underestimated compared with the experiment in the range  $1.3 \leq \Delta u \leq 2.2$  mm. Similarly, Dataset 2 (Fig. 7(b)) shows good agreement between simulated and experimental data. For  $\Delta u \geq 2.5$  mm simulated results for Dataset 2 slightly overestimate the force compared to the experiment. The overestimation is most notable at the final displacement point. The parameter values selected by the BO framework are provided in Table 3 for each of the three datasets analysed.

The tests for Dataset 1 and 2 have been carried out under nominally identical conditions, while the test for Dataset 3 has been carried out at a different temperature on the same material.

The statistical nature of material testing, often termed material scatter, has been widely acknowledged in the field of material science (O'Connor et al., 2022), so it is not unexpected that Dataset 1 and 2 provide different calibrations to the GTN model. Indeed machine learning methods such as the ones employed here may be a useful tool to identify the reasons behind such experimental scatter. However, the limited data available in the current study are not sufficient, as such a study would require many repeat tests.

It is interesting to note that parameter  $m$ , the slope of the extrapolated true stress–true strain curve was found to differ significantly between Datasets 1 and 2 (534 MPa and 725 MPa, respectively), although the load–displacement curves in Fig. 1 are quite similar and almost identical below maximum load. It is also interesting to note that the parameter  $f_0$ , initial void volume fraction, is very similar for all three datasets (0.137%, 0.134%, 0.131% for Dataset 1, 2 and 3, respectively). Generally the initial void volume fraction is not expected to vary significantly from specimen to specimen for a given material, which is consistent with what is observed here. However, parameters  $\epsilon_N$ ,  $S_N$  and  $f_N$ , which control void nucleation, are also expected to be constant for a given material (at a given temperature), so the values for Dataset 1 and 2 would be expected to be similar. However, as seen in Table 3 there are significant differences, e.g.  $f_N = 0.0387$  and  $0.0848$  for Dataset 1 and 2, respectively.

In terms of the fitting parameters ( $q_1$ ,  $q_2$  and  $q_3$ ) it is common practice to fix  $q_3 = q_1^2$  (Abbasi et al., 2011; Rousselier, 2019; Yan et al., 2021), based on assumptions in the original model (Tvergaard, 1981). In this work,  $q_3$  was not constrained and, as shown in Table 3, Dataset 2  $q_3 \approx q_1^2$ , but the relationship does not hold for the other two datasets. Again, for definitive statement in relation to the significance of parameter values, a much larger data set would be needed, which is not the purpose of the current analysis.

### 5.1. Effect of varying BO hyperparameters

To assess the effect of hyperparameter selection on the model parameters, four BO analyses were performed on Dataset 1. For each analysis the acquisition function,  $\alpha_{UCB}$  (see Section 3.3), hyperparameter values  $N_R$  and  $N_O$  were varied, as shown in Table 4. The

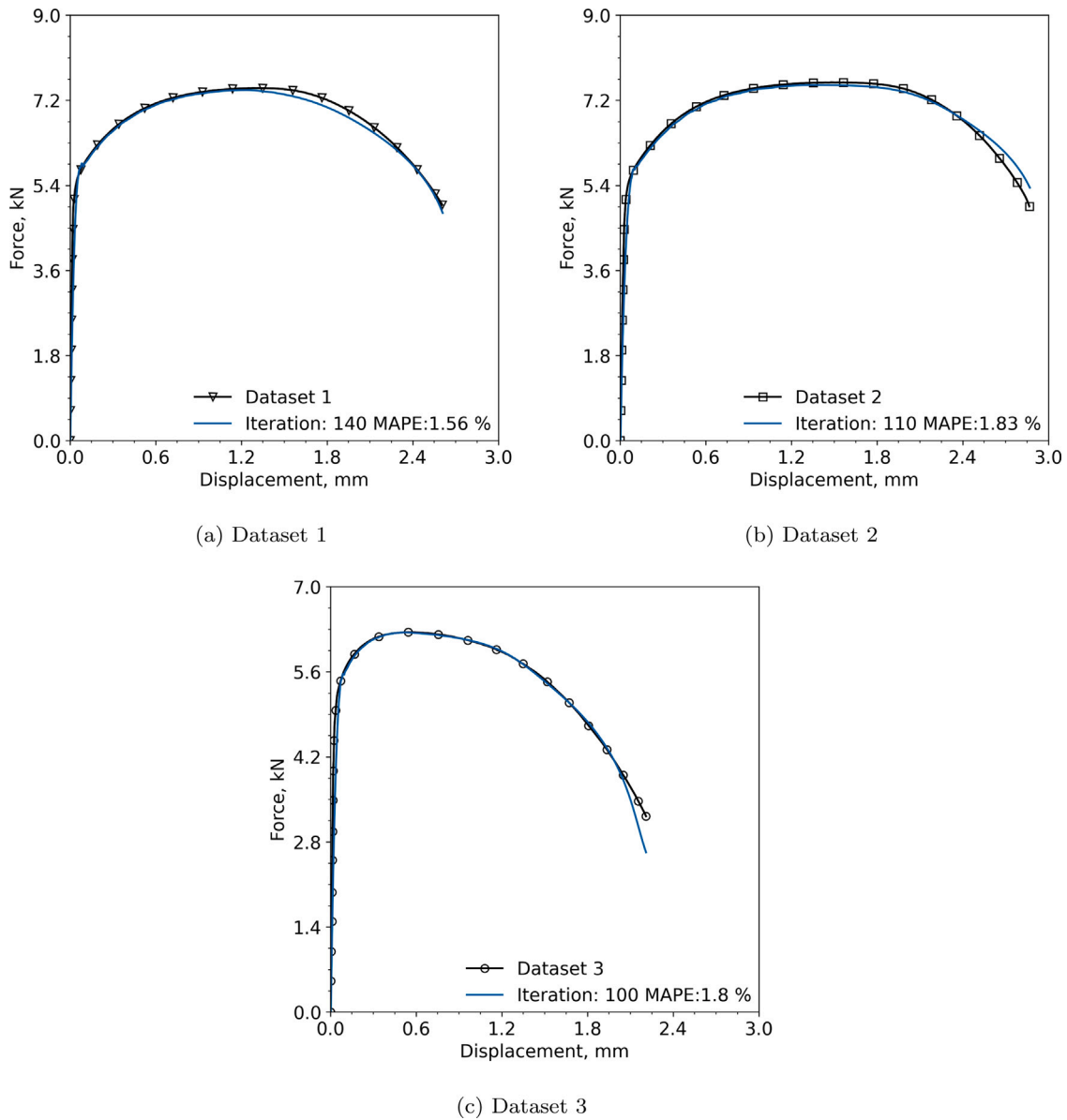


Fig. 7. Comparison of experimental test data to simulated output for Dataset 1 7(a), Dataset 2 7(b), and Dataset 3 7(c). Parameter values are shown in Table 3.

Table 4

Bayesian optimisation framework parameter values for dataset 1. The effect of hyperparameter settings on GTN parameter values.

Parameter	$H_1$	$H_2$	$H_3$	$H_4$
$N_O$	500	100	500	100
$N_R$	50,000	50,000	10,000	10,000
$q_1$	1.332	1.178	1.291	1.158
$q_2$	$9.952 \times 10^{-1}$	1.021	$9.547 \times 10^{-1}$	1.037
$q_3$	2.295	1.344	2.254	1.070
$\epsilon_N$	$2.900 \times 10^{-2}$	$3.598 \times 10^{-1}$	$3.519 \times 10^{-1}$	$3.331 \times 10^{-1}$
$s_N$	$1.671 \times 10^{-1}$	$1.580 \times 10^{-1}$	$1.001 \times 10^{-1}$	$1.234 \times 10^{-1}$
$f_N$	$3.869 \times 10^{-2}$	$5.769 \times 10^{-2}$	$3.086 \times 10^{-2}$	$7.594 \times 10^{-2}$
$f_0$	$1.370 \times 10^{-3}$	$1.431 \times 10^{-3}$	$1.412 \times 10^{-3}$	$1.309 \times 10^{-3}$
$m$	534.1	542.8	514.5	621.9
MAPE	1.563	1.614	1.398	1.105
$N_j$	140	133	46	130

load–displacement curves for the four cases are shown in Fig. 8. Excellent agreement with experimental data is achieved for the four hyperparameter choices.

It may be noted from Table 4 that all the model parameters depend on the hyperparameter selection. Given that excellent agreement was achieved for all four analyses this implies that the problem does not have a unique solution. That is to say that multiple combinations of the eight model parameters provide good agreement to the experimental data.

The issue of non-uniqueness in GTN model parameter values has been highlighted previously (Ryan et al., 2022; Kiran and Khandelwal, 2014; Brocks, 2018). One method of uniquely identifying GTN parameters is to examine a second or even third test specimen geometry. As the GTN model, Eq. (1), is not specimen specific the model parameters should be applicable to any geometry. The proposed framework, can be extended to include multiple specimen types, by, for example, obtaining a range of potential GTN model parameters from one specimen type, carrying out a second BO analysis on the second specimen type within this range, and continuing with other specimen types until a unique set of parameters is achieved. Due to constraints surrounding material availability, it was not possible to implement this approach with the current datasets.

One of the key targets of this work was to minimise the number of expensive evaluations (i.e. simulations) required. This informed

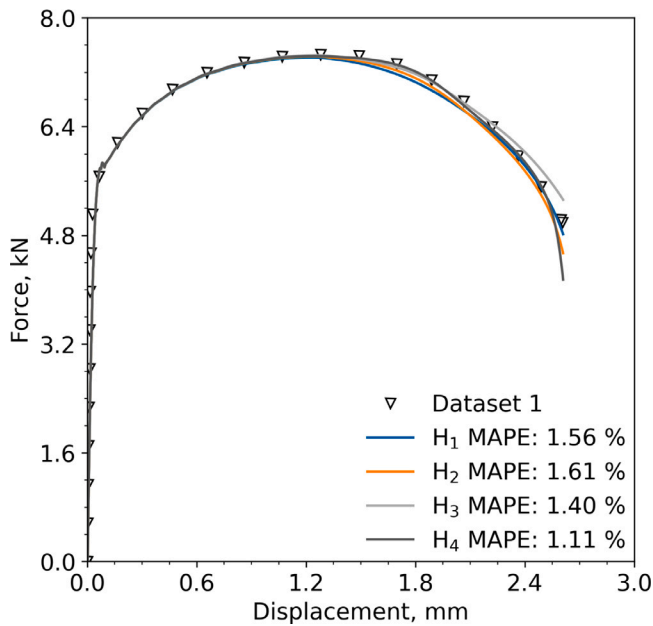


Fig. 8. Plot of force versus displacement showing experimental data and simulated output for various hyperparameters.

the initial selection of a two level DoE array where each parameter was assessed based on the maximum and minimum bounds. While increasing the level (on either one or more parameters) would provide a better initial estimate of the surrogate function, other model parameters such as the covariance and acquisition functions, have a much greater impact on model output (Rasmussen and Williams, 2006; Duvenaud, 2014). Increasing the number of DoE levels increases the initial number of expensive evaluations but does not necessarily reduce the number of iterations required by the BO framework. Hence a two level DoE is considered sufficient for the purposes of this work where a key target is to minimise the number of expensive evaluations.

### 5.2. Assessing non-uniqueness using Compact Tension geometry

The previous section demonstrates that modifying the Bayesian optimisation algorithm hyperparameters results in the selection of different GTN model parameter values for an individual dataset. Fig. 8 shows that despite the different GTN model parameters simulated uniaxial tensile load–displacement results are similar. The GTN model parameter values relate to the material in use and as such can be considered geometry independent (Brocks et al., 1995). CT specimens are a common standardised geometry used in fracture toughness testing (Institute, 2016). Plastic flow, in the mid-thickness of notched geometries, is constrained resulting in a triaxial stress state (Anderson, 2017). A triaxial stress state ensures that fracture toughness measurements from standard specimen geometries are conservative from a fracture perspective (O'Connor et al., 2022). In fracture toughness testing of ductile materials high stress triaxiality promotes void growth (Brocks, 2018), indicating that notched geometries like CT specimens may offer a potential solution to the non-uniqueness demonstrated in Fig. 8.

To assess whether a unique solution could be ascertained, FE simulations on a compact tension (CT) geometry were conducted. No relevant experimental data are available so what follows is a computational study only. A standard CT geometry, Fig. 9, was idealised to a 2D geometry using a plane strain assumption. The dashed red line shown in Fig. 9 represents the symmetry plane ( $U_1=U_3=0$ ). A displacement of 2.5 mm was applied to a reference node, located in the centre of the

loading hole ( $U_1=0$ ,  $U_2=2.5$ ). The geometry was meshed using 13765 CPE4R elements. Simulations were conducted using Abaqus/Standard implicit solver (Systemes, 2021).

The CT simulation load–displacement results are plotted in Fig. 10. As expected, the load–displacement traces are broadly similar up to a displacement value corresponding to the material UTS. Post-UTS simulation results for H2 and H3 diverge appreciably. Simulated results for simulations H1 and H4 appear broadly similar to one another but simulation H4 achieves a lower load, compared to that achieved for simulation H1, at the final applied displacement. These results indicate that the Bayesian optimised GTN parameter values could be used, in conjunction with experimental data, to find a unique set of GTN parameter values. Unfortunately, experimental test data for the CT geometry is not available for this work. As such it is not possible to state conclusively which of the GTN model parameter combinations applied here are the most appropriate. These results however do indicate that a non-unique solution can be potentially identified from data generated using the proposed framework if multiple test geometries are examined.

## 6. Conclusions

- A Bayesian optimisation framework successfully determined an array of eight material parameter values that, when applied to a ductile damage model simulation, produced an accurate representation of experimental tensile data with a mean average percentage error (MAPE) of less than 2%.
- The framework is fully autonomous requiring minimal user interaction and with the combined machine learning-finite element tool typically provides calibration values in less than four hours. This compares favourably with typical time spent on trial-and-error calibration for this model.
- The ductile model parameter values are found to be non-unique and it is shown that by changing the hyperparameters of the acquisition function, different combinations of ductile damage parameters are obtained.
- While a unique set of ductile damage parameters cannot be found from uni-axial tensile simulations alone, the application of a second test geometry can offer a potential solution to the uniqueness issue.

## Declaration of competing interest

The authors declare the following financial interests/personal relationships which may be considered as potential competing interests: Alison O'Connor reports financial support was provided by European Commission.

## Data availability

Additional supplementary information such as data files and code are available from zenodo <https://doi.org/10.5281/zenodo.7686217>.

## Acknowledgements

This work was funded by the European Union through the Marie Skłodowska-Curie Actions grant number 101028291. We acknowledge William Brennan, a University of Limerick undergraduate student, for his contributions to this research. We gratefully acknowledge helpful conversations with Dr Meghana Kshiragar and Ms Gauri Vaidya from the University of Limerick's Lero Centre. We also acknowledge members of the University of Limerick, Mathematics Applications Consortium for Science and Industry (MACSI) group for their insightful and supportive comments surrounding this research.



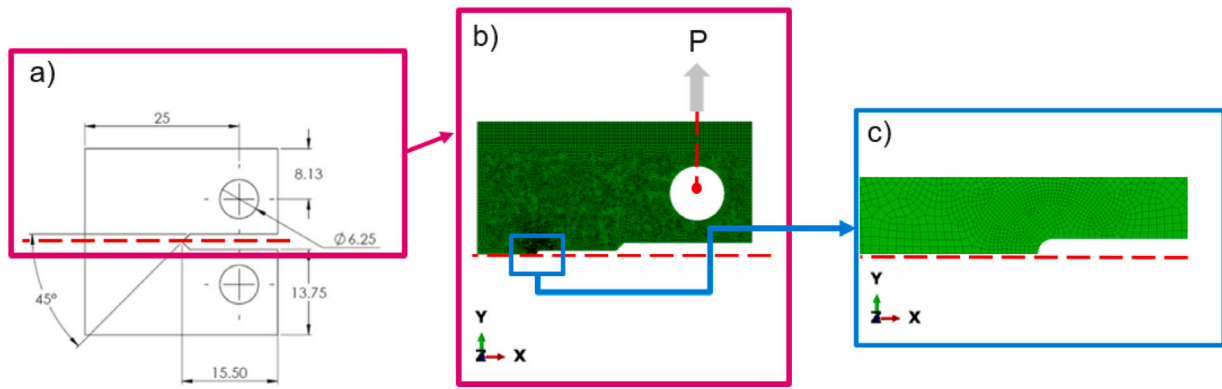


Fig. 9. Illustration detailing idealised compact tension FE model. (a) Technical drawing representative of geometry, dimensions in mm. (b) Idealised 2D plane strain model with illustrations detailing the location of boundary conditions. (c) Detailed view of meshing close to the notch tip.

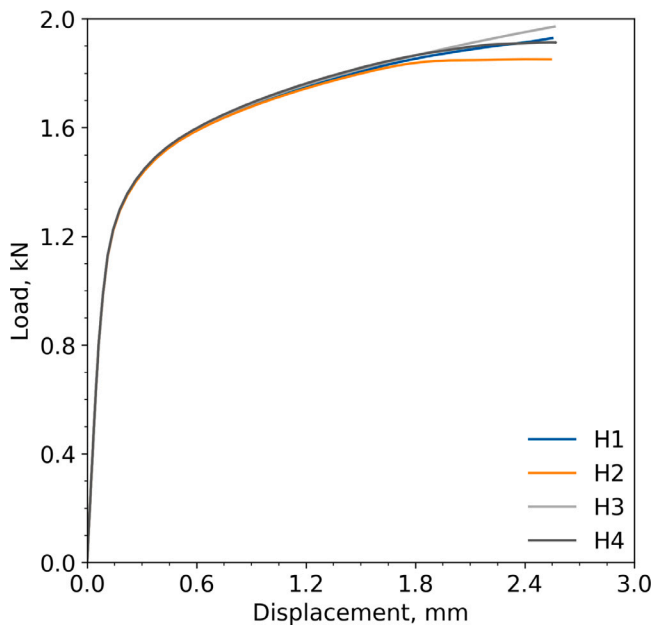


Fig. 10. Plot of force versus displacement for compact tension simulations.

## Appendix. Supplementary information

A preprint of this research is available (O'Connor et al., 2023). Additional supplementary information such as data files and code are available from zenodo <https://doi.org/10.5281/zenodo.7686217>.

```

1 from sklearn.linear_model import LinearRegression
2 import numpy as np
3 def estimate_max_slope(strain=None, stress=None):
4     """
5     :param strain: pandas series of true strain
6     :param stress: pandas series of true stress
7     :return: maximum slope value to nearest 100
8     """
9     for i in range(2, 7, 1):
10         x = strain[-i:].values.reshape(-1, 1)
11         y = stress[-i:].values.reshape(-1, 1)
12         model = LinearRegression().fit(x, y)
13         current_slope = model.coef_[0][0]
14         if i==2:
15             max_slope = current_slope
16         elif current_slope > max_slope:
17             max_slope = current_slope
18     return np.ceil(max_slope / 100) * 100
19

```

Listing 1: Function used to calculate maximum slope

## References

- Abbasi, M., Ketabchi, M., Izadkhah, H., Fatmehsaria, D.H., Aghbash, A.N., 2011. Identification of GTN model parameters by application of response surface methodology. 11th International Conference on the Mechanical Behavior of Materials (ICM11), Procedia Eng. 11th International Conference on the Mechanical Behavior of Materials (ICM11), 10, 415–420. <http://dx.doi.org/10.1016/j.proeng.2011.04.070>.
- Abbassi, F., Belhadj, T., Mistou, S., Zghal, A., 2013. Parameter identification of a mechanical ductile damage using Artificial Neural Networks in sheet metal forming. Mater. Des. 45, 605–615. <http://dx.doi.org/10.1016/j.matdes.2012.09.032>.
- Abbassi, F., Karrech, A., Islam, M.S., Seibi, A.C., 2023. Poromechanics of fractured/faulted reservoirs during fluid injection based on continuum damage modeling and machine learning. Nat. Resour. Res. 32 (1), 413–430. <http://dx.doi.org/10.1007/s11053-022-10134-8>.
- Abendroth, M., Kuna, M., 2006. Identification of ductile damage and fracture parameters from the small punch test using neural networks. Eng. Fract. Mech. 73 (6), 710–725. <http://dx.doi.org/10.1016/j.engfracmech.2005.10.007>.
- Anderson, T.L., 2017. Fracture Mechanics: Fundamentals and Applications, fourth ed. Taylor & Francis, Boca Raton, FL.
- Anon, 2019. EN ISO 6892-1:2019 Metallic Materials - Tensile Testing - Part 1: Method of Test at Room Temperature (ISO 6892-1:2019). European Committee for Standardization (CEN).
- Bikmukhametov, T., Jäschke, J., 2020. Combining machine learning and process engineering physics towards enhanced accuracy and explainability of data-driven models. Comput. Chem. Eng. 138, 106834. <http://dx.doi.org/10.1016/j.compchemeng.2020.106834>.
- Borowska, A., Gao, H., Lazarus, A., Husmeier, D., 2022. Bayesian optimisation for efficient parameter inference in a cardiac mechanics model of the left ventricle. Int. J. Numer. Methods Biomed. Eng. 38 (5), e3593. <http://dx.doi.org/10.1002/cnm.3593>.
- Brocks, W., 2018. Plasticity and Fracture. In: Solid Mechanics and Its Applications. Vol. 244, first ed. Springer International Publishing, Cham, <http://dx.doi.org/10.1007/978-3-319-62752-6>.
- Brocks, W., Klingbeil, D., Künneke, G., Sun, D.-Z., 1995. Application of the Gurson model to ductile tearing resistance. In: Bakker, A. (Ed.), Constraint Effects in Fracture Theory and Applications: Second Volume. ASTM International, West Conshohocken, PA, pp. 232–252. <http://dx.doi.org/10.1520/STP146388>.
- Chahboub, Y., Szavai, S., 2019. Determination of GTN parameters for SENT specimen during ductile fracture. In: Procedia Structural Integrity. Vol. 16. Elsevier B.V., pp. 81–88. <http://dx.doi.org/10.1016/j.prostr.2019.07.025>.
- Chen, D., Li, Y., Yang, X., Jiang, W., Guan, L., 2021. Efficient parameters identification of a modified GTN model of ductile fracture using machine learning. Eng. Fract. Mech. 245, 107535. <http://dx.doi.org/10.1016/j.engfracmech.2021.107535>.
- Chuaqui, T.R.C., Rhead, A.T., Butler, R., Scarth, C., 2021. A data-driven Bayesian optimisation framework for the design and stacking sequence selection of increased notched strength laminates. Composites B 226, 109347. <http://dx.doi.org/10.1016/j.compositesb.2021.109347>.
- De Ath, G., Everson, R.M., Rahat, A.A.M., Fieldsend, J.E., 2021. Greed is Good: Exploration and exploitation trade-offs in Bayesian optimisation. ACM Trans. Evol. Learn. Optim. 1 (1), 1–22. <http://dx.doi.org/10.1145/3425501>, arXiv:1911.12809.
- Dewancker, I., McCourt, M., Clark, S., 2016. Bayesian optimization for machine learning: A practical guidebook. arXiv:1612.04858 [cs].
- Duvenaud, D., 2014. Automatic Model Construction with Gaussian Processes (Ph.D. thesis). University of Cambridge, <http://dx.doi.org/10.17863/CAM.14087>.
- Ertel, W., 2017. Introduction to Artificial Intelligence. In: Undergraduate Topics in Computer Science, Springer International Publishing, Cham, <http://dx.doi.org/10.1007/978-3-319-58487-4>.

- Fraley, S., Oom, M., Terrien, B., Zalewski, J., 2020. 14.1: Design of experiments via taguchi methods - orthogonal arrays. In: Chemical Process Dynamics and Controls. URL [https://eng.libretexts.org/Bookshelves/Industrial\\_and\\_Systems\\_Engineering/Book%3A\\_Chemical\\_Process\\_Dynamics\\_and\\_Controls\\_\(Woelfl\)/14%3A\\_Design\\_of\\_Experiments/14.01%3A\\_Design\\_of\\_Experiments\\_via\\_Taguchi\\_Methods\\_-\\_Orthogonal\\_Arrays](https://eng.libretexts.org/Bookshelves/Industrial_and_Systems_Engineering/Book%3A_Chemical_Process_Dynamics_and_Controls_(Woelfl)/14%3A_Design_of_Experiments/14.01%3A_Design_of_Experiments_via_Taguchi_Methods_-_Orthogonal_Arrays).
- Ghavamian, F., 2021. Accelerating finite element analysis using machine learning. <http://dx.doi.org/10.4233/uuid:015bbf35-5e29-4630-b466-1a29d4c5bfb3>.
- Gunn, B., Hettiarachchi, I.T., Johnstone, M., Le, V., Creighton, D., Preston, L., 2022. Improving high value manufacturing with simulation-based Bayesian Optimisation. In: 2022 IEEE International Systems Conference (SysCon). pp. 1–8. <http://dx.doi.org/10.1109/SysCon53536.2022.9773798>.
- Gurson, A.L., 1977. Continuum theory of ductile rupture by void nucleation and growth: Part I—Yield criteria and flow rules for porous ductile media. *J. Eng. Mater. Technol.* 99 (1), 2–15. <http://dx.doi.org/10.1115/1.3443401>.
- Hegde, J., Rokseth, B., 2020. Applications of machine learning methods for engineering risk assessment – A review. *Saf. Sci.* 122, 104492. <http://dx.doi.org/10.1016/j.ssci.2019.09.015>.
- Institute, B.S., 2016. ISO 12135:2016 Metallic materials. Unified method of test for the determination of quasistatic fracture toughness. URL <https://bsol.bsigroup.com/Bibliographic/BibliographicInfoData/000000000030293840>.
- Kiran, R., Khandelwal, K., 2014. Gurson model parameters for ductile fracture simulation in ASTM A992 steels. *Fatigue Fract. Eng. Mater. Struct.* 37 (2), 171–183. <http://dx.doi.org/10.1111/ffe.12097>.
- Li, X., Li, Z., Chen, Y., Zhang, C., 2023. An enhanced data-driven constitutive model for predicting strain-rate and temperature dependent mechanical response of elastoplastic materials. *Eur. J. Mech. A Solids* 100, 104996. <http://dx.doi.org/10.1016/j.euromechsol.2023.104996>.
- Liang, Q., Gongora, A.E., Ren, Z., Tihiainen, A., Liu, Z., Sun, S., Deneault, J.R., Bash, D., Mekki-Berrada, F., Khan, S.A., Hippalgaonkar, K., Maruyama, B., Brown, K.A., Fisher III, J., Buonassisi, T., 2021. Benchmarking the performance of Bayesian optimization across multiple experimental materials science domains. *NPJ Comput. Mater.* 7 (1), 1–10. <http://dx.doi.org/10.1038/s41524-021-00656-9>.
- Liu, X., Athanasiou, C.E., Padture, N.P., Sheldon, B.W., Gao, H., 2020. A machine learning approach to fracture mechanics problems. *Acta Mater.* 190, 105–112. <http://dx.doi.org/10.1016/j.actamat.2020.03.016>.
- Maire, E., Bouaziz, O., Di Michiel, M., Verdu, C., 2008. Initiation and growth of damage in a dual-phase steel observed by X-ray microtomography. *Acta Mater.* 56 (18), 4954–4964. <http://dx.doi.org/10.1016/j.actamat.2008.06.015>.
- Meade, E.D., 2020. Experimental Study & Multiscale Modelling of the High Temperature Deformation of P91 under Multiaxial Loading (Ph.D. thesis). University of Limerick.
- Mongan, P.G., Modi, V., McLaughlin, J.W., Hinchey, E.P., O'Higgins, R.M., O'Dowd, N.P., McCarthy, C.T., 2022. Multi-objective optimisation of ultrasonically welded dissimilar joints through machine learning. *J. Intell. Manuf.* 33 (4), 1125–1138. <http://dx.doi.org/10.1007/s10845-022-01911-6>.
- Nasiri, S., Khosravani, M.R., Weinberg, K., 2017. Fracture mechanics and mechanical fault detection by artificial intelligence methods: A review. *Eng. Fail. Anal.* 81, 270–293. <http://dx.doi.org/10.1016/j.engfailanal.2017.07.011>.
- O'Connor, A.N., Davies, C.M., Garwood, S.J., 2022. The influence of constraint on fracture toughness: Comparing theoretical T0 shifts in master curve analyses with experimental data. *Eng. Fract. Mech.* 275, 108857. <http://dx.doi.org/10.1016/j.engfracmech.2022.108857>.
- O'Connor, A., Mongan, P., O'Dowd, N., 2023. A Machine Learning Approach to Automate Ductile Damage Parameter Selection in Finite Element Simulations. Zenodo, <http://dx.doi.org/10.5281/zenodo.7620179>.
- Pedregosa, F., Varoquaux, G., Gramfort, A., Michel, V., Thirion, B., Grisel, O., Blondel, M., Prettenhofer, P., Weiss, R., Dubourg, V., Vanderplas, J., Passos, A., Cournapeau, D., Brucher, M., Perrot, M., Duchesnay, É., 2011. Scikit-learn: Machine learning in Python. *J. Mach. Learn. Res.* 12 (85), 2825–2830, URL <http://jmlr.org/papers/v12/pedregosa11a.html>.
- Rasmussen, C.E., 2004. Gaussian processes in machine learning. In: Bousquet, O., von Luxburg, U., Rätsch, G. (Eds.), *Advanced Lectures on Machine Learning: ML Summer Schools 2003*, Canberra, Australia, February 2 - 14, 2003, Tübingen, Germany, August 4 - 16, 2003, Revised Lectures. In: *Lecture Notes in Computer Science*, Springer, Berlin, Heidelberg, pp. 63–71. [http://dx.doi.org/10.1007/978-3-540-28650-9\\_4](http://dx.doi.org/10.1007/978-3-540-28650-9_4).
- Rasmussen, C.E., Williams, C.K.I., 2006. *Gaussian Processes for Machine Learning*. In: *Adaptive Computation and Machine Learning*, MIT Press, Cambridge, Mass.
- Rousselier, G., 2019. Modeling of Plasticity and Ductile Fracture Physical Mechanisms and Numerical Simulation of Laboratory Specimens. Technical Report, p. 15.
- Ryan, S., Berk, J., Rana, S., McDonald, B., Venkatesh, S., 2022. A Bayesian optimisation methodology for the inverse derivation of viscoplasticity model constants in high strain-rate simulations. *Def. Technol.* 18 (9), 1563–1577. <http://dx.doi.org/10.1016/j.dt.2021.10.013>.
- Schulte, R., Karca, C., Ostwald, R., Menzel, A., 2023. Machine learning-assisted parameter identification for constitutive models based on concatenated loading path sequences. *Eur. J. Mech. A Solids* 98, 104854. <http://dx.doi.org/10.1016/j.euromechsol.2022.104854>.
- Shahriari, B., Swersky, K., Wang, Z., Adams, R.P., de Freitas, N., 2016. Taking the human out of the loop: A review of Bayesian optimization. *Proc. IEEE* 104 (1), 148–175. <http://dx.doi.org/10.1109/JPROC.2015.2494218>.
- Systemes, D., 2021. Abaqus/CAE User's Guide - SIMULIA User Assistance 2021. Dassault Systemes, URL [https://help.3ds.com/2020/English/DSSIMULIA\\_Established](https://help.3ds.com/2020/English/DSSIMULIA_Established).
- Tvergaard, V., 1981. Influence of voids on shear band instabilities under plane strain conditions. *Int. J. Fract.* 17 (4), 389–407. <http://dx.doi.org/10.1007/BF00036191>.
- Tvergaard, V., Needleman, A., 1984. Analysis of the cup-cone fracture in a round tensile bar. *Acta Metall.* 32 (1), 157–169. [http://dx.doi.org/10.1016/0001-6160\(84\)90213-X](http://dx.doi.org/10.1016/0001-6160(84)90213-X).
- Uy, M., Telford, J.K., 2009. Optimization by design of experiment techniques. In: 2009 IEEE Aerospace Conference. pp. 1–10. <http://dx.doi.org/10.1109/AERO.2009.4839625>.
- Wankerl, H., Wiesmann, C., Kreiner, L., Butendeich, R., Luce, A., Sobczyk, S., Stern, M.L., Lang, E.W., 2022. Directional emission of white light via selective amplification of photon recycling and Bayesian optimization of multi-layer thin films. *Sci. Rep.* 12 (1), 5226. <http://dx.doi.org/10.1038/s41598-022-08997-1>.
- Weislik, W., 2016. Experimental determination of critical void volume fraction ff for the Gurson Tvergaard Needleman (GTN) model. 21st European Conference on Fracture, ECF21, 20-24 June 2016, Catania, Italy, Procedia Struct. Integr. 21st European Conference on Fracture, ECF21, 20-24 June 2016, Catania, Italy, 2, 1676–1683. <http://dx.doi.org/10.1016/j.prostr.2016.06.212>.
- Yan, R., Xin, H., Veljkovic, M., 2021. Ductile fracture simulation of cold-formed high strength steel using GTN damage model. *J. Constr. Steel Res.* 184, 106832. <http://dx.doi.org/10.1016/j.jcsr.2021.106832>.
- Zhang, Y., Apley, D.W., Chen, W., 2020. Bayesian optimization for materials design with mixed quantitative and qualitative variables. *Sci. Rep.* 10 (1), 1–13. <http://dx.doi.org/10.1038/s41598-020-60652-9>.
- Zhang, T., Lu, K., Mano, A., Yamaguchi, Y., Katsuyama, J., Li, Y., 2021. A novel method to uniquely determine the parameters in Gurson-Tvergaard-Needleman model. *Fatigue Fract. Eng. Mater. Struct.* 44 (12), 3399–3415. <http://dx.doi.org/10.1111/ffe.13568>.
- Zhu, C., Byrd, R.H., Lu, P., Nocedal, J., 1997. Algorithm 778: L-BFGS-B: Fortran subroutines for large-scale bound-constrained optimization. *ACM Trans. Math. Software* 23 (4), 550–560. <http://dx.doi.org/10.1145/279232.279236>.